

# MODEL ATMOSPHERES FOR IRRADIATED STARS IN PRE-CATAclysmic VARIABLES

TRAVIS S. BARMAN

Department of Physics, Wichita State University, Wichita, KS 67260-0032  
 Email: [travis.barman@wichita.edu](mailto:travis.barman@wichita.edu)

PETER H. HAUSCHILDT

Hamburger Sternwarte, Gojenbergsweg 112, 21029 Hamburg, Germany  
 Email: [yeti@hs.uni-hamburg.de](mailto:yeti@hs.uni-hamburg.de)

FRANCE ALLARD

C.R.A.L, Ecole Normale Supérieure, 69364 Lyon Cedex 7, France  
 Email: [fallard@ens-lyon.fr](mailto:fallard@ens-lyon.fr)

*Accepted for publication in the ApJ: June 24, 20004*

## ABSTRACT

Model atmospheres have been computed for M dwarfs that are strongly irradiated by nearby hot companions. A variety of primary and secondary spectral types are explored in addition to models specific to four known systems: GD 245, NN Ser, AA Dor, and UU Sge. This work demonstrates that a dramatic temperature inversion is possible on at least one hemisphere of an irradiated M dwarf and the emergent spectrum will be significantly different from an isolated M dwarf or a black body flux distribution. For the first time, synthetic spectra suitable for direct comparison to high-resolution observations of irradiated M dwarfs in non-mass transferring post-common envelope binaries are presented. The effects of departures from local thermodynamic equilibrium on the Balmer line profiles are also discussed.

*Subject headings:* stars: atmospheres, binaries: close, radiative transfer

## 1. INTRODUCTION

Synthetic spectra from model atmospheres are frequently used in the analysis of observed spectroscopic and photometric data. For the most part, the models are sufficiently detailed to test the current theoretical understanding of stellar and sub-stellar mass objects at various stages in their evolution. However, the majority of model atmospheres are intended for comparisons to isolated stars and are not appropriate for many short period binaries. A number of binary systems have orbital separations small enough so that one of the binary members is significantly heated by its companion. In order for synthetic spectra to be useful in such cases, the standard “isolated” modeling approach must be replaced by one that includes the effects of irradiation.

Post-common envelope binaries (PCEBs) are examples of systems where large effects due to irradiation have been observed (e.g. Z Cha, Wade & Horne (1988); GD 245, Schmidt et al. (1995); GD 444, Marsh & Duck (1996)). Many PCEBs are cataclysmic variables (CVs) with secondaries that, in addition to being irradiated, have over filled their Roche lobe and transfer mass to the primary via accretion streams or a disk. CVs, while very interesting, are not necessarily the best choice for studying the effects of irradiation on cool stars. PCEBs that do not have on-going mass exchange offer several advantages. The absence of accretion ensures that the primary is the only major source of external heating for the secondary. CVs have additional sources of radiation energy (e.g., from the accretion disk) that are complicated to model and could lead to shadows or bright spots on the secondary. An additional advantage of PCEBs without

mass exchange is that the secondaries have not over filled their Roche lobe and are therefore more spherical. Most non-mass transferring PCEBs are labeled pre-CVs and often contain a main sequence (MS) star in close orbit around a much hotter white dwarf (WD) or sub-dwarf (sdOB). The current study will be restricted to pre-CVs with orbital periods less than 16 days or orbital separations less than about  $3R_{\odot}$  (i.e., those that could possibly become a CV within a Hubble time; Hillwig et al. (2000)). For an excellent review of detached binaries containing WD primaries, see (Marsh 2000).

The average effective temperature of the primary (the WD or sdOB) in pre-CVs is about 50,000K with a few reaching 100,000K. At just a few  $R_{\odot}$  away, the much cooler secondary star is significantly heated by the primary’s radiation. Therefore, the secondary’s irradiated atmosphere is regulated by both *extrinsic* radiation from the primary and *intrinsic* energy supplied by internal nuclear reactions (or, in the case of a brown dwarf secondary, leftover gravitational energy from formation). Depending on the temperatures, pressures, and chemical composition of the secondary’s atmosphere, a fraction of the extrinsic radiation will be reflected via scattering by grains, molecules or electrons (or a combination of these) while the remaining is absorbed and re-radiated. Furthermore, the two sources of energy may have spectral energy distributions (SEDs) that peak at very different wavelengths which implies that a broader category of opacity sources (spanning the EUV to the far IR) become important in shaping the secondary’s atmospheric structure and emergent spectrum. The situation is also complicated by the fact that only one hemisphere of the irradiated companion is heated at any given time.

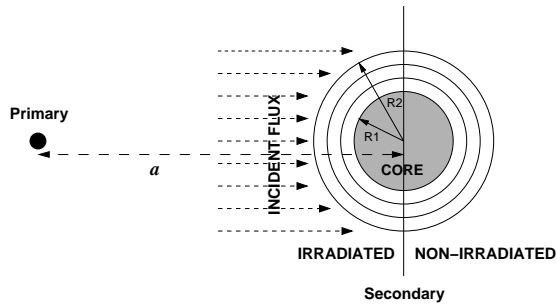


FIG. 1.— An illustration of the irradiation model. The primary (left) is treated as a point source at distance  $a$  from the center of the secondary (right). The secondary is divided into two hemispheres: irradiated and non-irradiated. The atmosphere on either hemisphere is modeled as a collection of concentric shells with the height of the atmosphere equal to  $R_2 - R_1$ .

Only a few theoretical studies applicable to the atmospheres and spectra of pre-CVs have been published. One of the more recent works investigated the effects of irradiation in the eclipsing binary BE Ursae Majoris using CLOUDY (Ferguson & James 1994). A narrow range of M dwarfs ( $3400\text{K} < T_{\text{eff}} < 3800\text{K}$ ) located near a  $10,000\text{K}$  black body have also been modeled (Brett & Smith 1993, here after BS93). A few earlier papers provided critical insight into the problem of irradiation but did not consider situations relevant for pre-CVs (Vaz & Nordlund 1985; Nordlund & Vaz 1990). In addition, the necessary opacity data and spectral line databases needed to compute realistic synthetic spectra were not available at the time. Consequently, no synthetic spectra have been published that are detailed enough to provide useful comparisons to high-resolution, phase-resolved, observations of pre-CVs. Furthermore, most light curve models continue to use black body SEDs or, at best, non-irradiated atmosphere models.

In the following sections, models for a variety of irradiated pre-CV secondaries will be presented. The changes in the atmospheric structure, the chemical composition, and the spectra will be described. Detailed, line-blanketed, synthetic spectra will also be presented for a few specific pre-CV systems.

## 2. MODEL CONSTRUCTION

All calculations presented here were produced using the PHOENIX model atmosphere code (Hauschildt & Baron 1999). PHOENIX includes an equation of state and radiative transfer solver that is suitable for modeling a broad range of both hot (Aufdenberg 2001) and cool (Allard et al. 2001) objects across the H-R diagram. This flexibility makes PHOENIX well suited for modeling systems that contain two extremely different objects (e.g. M dwarfs and WDs).

The secondary may be conceptually divided into two distinct hemispheres; irradiated and non-irradiated (see Figure 1). The irradiated hemisphere receives incoming radiation over all angles between  $0^\circ$  and  $90^\circ$  with respect to the surface normal. The effects of heating by the primary will vary across the surface with decreased heating near the boundary between the two hemispheres. In order to simplify the simulations, each hemisphere was modeled separately using a 1-D, spherically symmetric, atmosphere designed to represent the *average* thermal

and spectroscopic properties. Since pre-CVs are non-mass transferring systems, the secondary does *not* overflow its Roche lobe and, hence, should be reasonably well approximated by a sphere. Consequently, the same mass and effective gravity (set at a reference optical depth) was used for both hemisphere models. However, despite having the same bulk properties, maintaining a consistent temperature structure and entropy ( $S$ ) at the bottom of both atmosphere models for the irradiated and non-irradiated hemispheres is not guaranteed. Differences between the temperature structures at the bottom of each model can exist because the effects of horizontal energy flow have not been included and the two hemispheres have been essentially decoupled. While horizontal energy flow is very likely to be present, including this in the simulations would require the solution of the full, multi-D, radiation-hydrodynamical problem that is currently beyond the scope of this paper. The standard approach for dealing with horizontal energy flow is to adjust the effective temperature of one model so the entropy at the deepest layer is the same for both hemispheres (Vaz & Nordlund 1985; BS93). The details of this problem and how it is handled are discussed in a subsequent section.

All models were computed assuming hydrostatic and radiative-convective equilibrium. Convection was included using the standard mixing length theory with the mixing length parameter set equal to two. The atmospheres were divided into 100 concentric shells and the spherically symmetric radiative transfer equation was solved while explicitly including the incident, frequency dependent, radiation field from the primary. Spherical symmetry, as opposed to the more traditional plane parallel geometry, was chosen because it provides a more realistic description of the incoming radiation at grazing angles that should not penetrate too deeply into the atmosphere. At some angles, the radiation can pass completely through the top of the atmosphere. The details of the radiative transfer solution may be found in Hauschildt & Baron (1999) (and refs. therein) and details of the irradiation are found in Barman et al. (2001, 2002); however, for clarity, a few of the important points are repeated.

A secondary with radius  $R_s$  intercepts an incident luminosity from a primary of radius  $R_p$  at distance  $d$  with flux  $F_p$  given by  $\pi R_s^2 \left(\frac{R_p}{d}\right)^2 F_p$ . This absorbed energy must be distributed over and re-radiated by some fraction of the full secondary surface area ( $4\pi R_s^2$ ). The three most commonly explored physical scenarios are re-radiation by the full surface area, by the irradiated hemisphere only, or by a single point. Since the models must conserve energy, the incoming luminosity must balance the out-going luminosity of re-radiated extrinsic energy. In which case,  $\pi R_s^2 \left(\frac{R_p}{d}\right)^2 F_p = \text{Area} \times F_{\text{out}}$ . If one further assumes that  $F_{\text{inc}} = F_{\text{out}}$ , the monochromatic incident fluxes can be expressed as,

$$F_{\text{inc},\lambda} = \alpha \left(\frac{R_p}{d}\right)^2 F_{p,\lambda}, \quad (1)$$

where  $F_{p,\lambda}$  are the monochromatic fluxes from the primary surface, and  $d$  is the distance from the primary surface to the secondary surface (note,  $d = a - R_p - R_s$ , where  $a$  is the orbital separation). The parameter  $\alpha$  sets

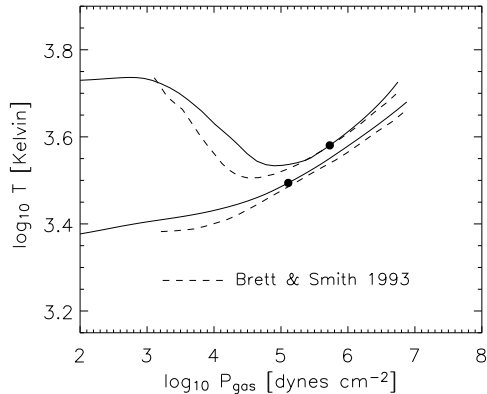


FIG. 2.— Temperature versus pressure for irradiated (top) and non-irradiated (bottom) atmosphere models. Solid lines are the results of PHOENIX simulations while dashed lines are taken from Fig. 3 of Brett & Smith (1993). Filled circles indicate the location of the radiative-convective boundary in the PHOENIX models. The differences between the two sets of calculation are most likely due to the different treatments of the equation of state and opacities.

the redistribution of the absorbed incident energy over the secondary's surface. All incident energy being absorbed and re-radiated by the heated hemisphere corresponds to  $\alpha = 0.5$ . Re-radiation by the entire secondary surface corresponds to  $\alpha = 0.25$  and  $\alpha = 1.0$  is for re-radiation by a single point on the surface. For a more detailed description of the energy balance in an irradiated binary companion and the development of a similar  $\alpha$  parameter, see Paczyński (1980). Unless otherwise stated, the models presented below were calculated with  $\alpha = 0.5$ . This choice is motivated by the fact that many short period binaries have tidally locked secondaries.

In all cases, the incident radiation was approximated by an isotropic radiation field consisting of 64 incoming intensities (corresponding to 64 incident angles) at the top most layer ( $\tau_{1.2} = 0$ , where  $\tau_{1.2}$  refers to a reference optical depth measured at  $1.2\mu\text{m}$ ) of the model. Isotropic illumination (instead of heating at a fixed angle) was chosen because it better approximates the situation illustrated in Fig. 1. While this is clearly a simplification of the true incident radiation, isotropy roughly accounts for the fact that the heated hemisphere receives radiation from the primary at all angles between 0 and 90 degrees (with respect to the surface normal). Even when the incident radiation is assumed to be isotropic, there are still benefits to using spherical geometry. Spherical geometry, combined with isotropic irradiation, accounts for the preferential heating of the upper atmospheric layers compared to the deeper layers for regions near the boundary between the two hemispheres. Across the heated hemisphere, the upper layers always receive extrinsic radiation while the deeper layers experience considerably less heating near the boundary compared to the substellar point. By virtue of the translational symmetry inherent in plane parallel models, *all* inward directed intensities are propagating toward the center of the object. Thus, for some situations, plane parallel geometry could overestimate the heating of deeper atmospheric layers and underestimate the heating of upper layers. The differences between plane parallel and spherical models are maxi-

mized when the atmospheric extension is large compared to the mean free path of a photon (e.g., in low gravity objects). For a spherical model, a large extension has the effect of decreasing the range of angles over which incident intensities actually propagate toward the bottom of the photosphere. In the future, the heated hemisphere will be modeled as a collection of small annular regions where the extrinsic radiation is incident along a single angle (or a narrow range). In this case, the advantages of spherical geometry over plane parallel will be even more significant.

Since pre-CV primaries have spectra that are very different from black body SEDs, the incident intensities were taken from synthetic WD spectra (also calculated with PHOENIX; Barman et al. 2000). In this way, a more realistic, wavelength dependent spectrum was used for the incoming radiation. Unless otherwise stated, the WD models have  $\log(g) = 8.0$  (cgs units),  $1 M_{\odot}$ , and  $10^{-2}$  solar metal abundances. When modeling a secondary for a specific pre-CV, a new model atmosphere and synthetic spectrum were used that closely match the primary spectral type and, if available, the observed fluxes.

The model calculations for both the primary and the secondary included more than 50,000 wavelength points between  $10\text{\AA}$  and  $1000\mu\text{m}$  with a resolution of about  $1\text{\AA}$  from the UV to the near-IR (this resolution may be increased as necessary). The equation of state and opacity setup was similar to that used in the NextGen model atmosphere grid of Hauschildt et al. (1999) but has since been updated to include more recent chemical and opacity data (Allard et al. 2001). Local thermodynamic equilibrium (LTE) was assumed for the majority of the calculations; however, the effects of non-LTE are explored for the hydrogen atom. All models for the secondaries used a solar composition that included 40 of the most important atomic elements from H to La (atomic numbers 1 through 57) as well as their important ions. The atomic data for the energy levels and bound-bound transitions are from Kurucz (1994) and Kurucz & Bell (1995). The molecular opacities include  $\text{H}_2\text{O}$  (Partridge & Schwenke 1997),  $\text{TiO}$  (Schwenke 1998),  $\text{VO}$  (linelist provided by R. Freedman, 2001, private communication) all diatomics from Kurucz (1993), and all lines from the HITRAN and GEISA databases (Rothman et al. 1992; Husson et al. 1992). Collision induced absorption (CIA) opacities are also included for  $\text{H}_2$ ,  $\text{N}_2$ ,  $\text{Ar}$ ,  $\text{CH}_4$ , and  $\text{CO}_2$  according to (Gruszka & Borysow 1997, and references therein). The total number of atomic and molecular lines currently available in PHOENIX (version 13) is  $\sim 700$  million. Scattering (Thomson, Rayleigh, and Mie) was also included and assumed to be isotropic.

The PHOENIX model atmosphere code uses the effective temperature as an input parameter that specifies (through the Stefan-Boltzmann formula) the net flux (or luminosity) that the model will have. To avoid confusion between the effective temperature of irradiated and non-irradiated models, the variable  $T_{\text{eff}}$  will be used only to refer to the effective temperature of non-irradiated models. In the case of irradiated models,  $T_{\text{int}}$  will be used to describe the *intrinsic* effective temperature; i.e. the effective temperature the model would have if irradiation was not present.

### 3. RESULTS

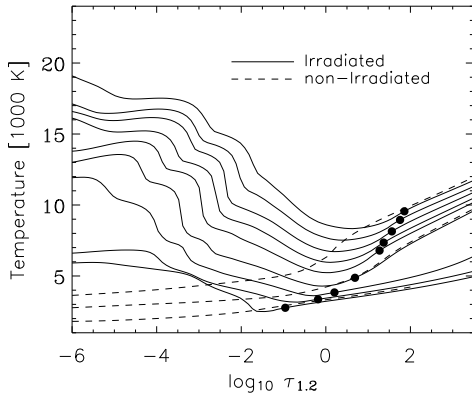


FIG. 3.— Temperature as a function of optical depth at  $1.2\mu\text{m}$  for irradiated (solid lines) and non-irradiated (dashed lines) atmospheres. The irradiated atmospheres have  $T_p = 20,000\text{K}$  to  $100,000\text{K}$  (from top to bottom) in steps of  $10,000\text{K}$ . For all irradiated models, the orbital separation is  $1 R_\odot$  and  $T_{\text{int}} = 3000\text{K}$ . The non-irradiated models have  $T_{\text{eff}} = 5600\text{K}$ ,  $4000\text{K}$ , and  $3000\text{K}$  (from top to bottom). Filled circles indicate the location of the radiative-convective boundary.

### 3.1. Comparison to the BS93 Results

Figure 2 compares the temperature-pressure (T-P) profiles of non-irradiated and irradiated models to similar calculations from BS93 (see their Fig. 3). The models have  $T_{\text{int}} = 3400\text{K}$ ,  $\log(g) = 5.0$  (cgs units) and  $M_s = 0.22 M_\odot$  (note, BS93 used plane parallel models and so  $M_s$  is irrelevant). The PHOENIX irradiated model included a primary located at an orbital separation of  $0.39 R_\odot$  with  $T_p = 10,000\text{K}$ ,  $R_p = 0.0319 R_\odot$ , and  $\alpha = 1.0$ . These parameters were chosen to match the incident flux used by BS93.

The models in Fig. 2 illustrate the basic properties of an irradiated atmosphere. As should be expected, substantial heating occurs in the upper layers of the irradiated atmosphere (low  $P_{\text{gas}}$ ) where temperatures exceed those in the non-irradiated case by  $3000\text{K}$  or more. The temperature also increases throughout the atmosphere, even at regions with high gas pressures, resulting in a different inner adiabat compared to the non-irradiated model (the reasons for this are discussed below). Also, the radiative-convective boundary nearly reaches  $P_{\text{gas}} \sim 10^6 \text{ dynes cm}^{-2}$  as convection retreats to deeper layers in the irradiated atmosphere.

Both PHOENIX and BS93 models predict a similar temperature inversion at the top of the irradiated atmosphere and similar adiabats at high  $P_{\text{gas}}$ . However, the BS93 profiles are noticeably cooler than the PHOENIX profiles at nearly all  $P_{\text{gas}}$ . Above the temperature minimum in the irradiated case (near  $P_{\text{gas}} = 10^5 \text{ dynes cm}^{-2}$ ), the temperatures are more than  $800\text{K}$  higher in the PHOENIX models. These differences are likely due to the use of “straight mean” (SM) molecular opacities and a lack of any atomic line opacity in the BS93 models. The lack of atomic line opacity can explain the differences at high pressures due to an underestimated backwarming affect. At low pressures, it is difficult to pinpoint the exact causes of the differences but, as pointed out by BS93, SM opacities tended to overblanket their models which could have caused preferential heating of the

outer layers. Note that, when the BS93 models were produced, reliable atomic and molecular line-lists were only just becoming available and thus the use of SM opacities was quite common. Large line databases, however, have been steadily produced over the past few years and are incorporated into PHOENIX using a direct opacity sampling method. A second major difference between the two sets of models is the completeness of the equation of state. PHOENIX includes a far greater number of species (literally many hundreds of molecules) in the solution of the chemical equilibrium equations compared to the BS93 models. Differences in the chemical equilibrium can lead to very different concentrations of primary opacity sources and ultimately very different temperature structures. Despite the differences between the models, the fact that two independent atmosphere codes produce qualitatively consistent results is encouraging.

### 3.2. Atmospheric Structures

To explore the effects of irradiation by primaries with different  $T_p$  values, a sequence of models was calculated for a secondary with  $T_{\text{int}} = 3000\text{K}$ ,  $\log(g) = 5.0$ ,  $M_s = 0.22 M_\odot$  and solar metallicities. The primary was a  $0.014 R_\odot$ ,  $\log(g) = 8.0$  (sub-solar metallicity) WD located  $1 R_\odot$  from the secondary.  $T_p$  was increased from  $20,000\text{K}$  to  $100,000\text{K}$  by steps of  $10,000\text{K}$ . With this setup, the incident flux spans almost 3 orders of magnitude with  $-0.7 \leq \log(F_{\text{inc}}/F_{\text{int}}) \leq 2.1$ .

The temperatures as functions of optical depth ( $\tau_{1.2}$ ) are shown in Fig. 3 for each irradiated model atmosphere. The models are fully converged (i.e., energy is conserved to better than 2% at all layers) and the atmospheric chemistry and opacities are consistent with the changes in temperature. For the lowest primary temperature ( $T_p = 20,000\text{K}$ ), a significant temperature inversion forms in the upper regions of the atmosphere while the deeper layers (near  $\tau_{1.2} = 1$ ) remain fairly similar to a non-irradiated atmosphere with  $T_{\text{eff}} = T_{\text{int}}$ . As  $T_p$  increases, the temperature inversion also increases and the temperature minimum moves to deeper layers. With  $T_p = 100,000\text{K}$ , the temperatures at the top of the atmosphere reach  $19,000\text{K}$  and the T-minimum is located at  $\tau_{1.2} < 1.0$ . Once  $T_p$  is higher than  $30,000\text{K}$ , the inner temperature profile is no longer similar to that of a standard M dwarf, despite the fact that  $T_{\text{int}}$  was held fixed for this sequence of models.

The large range of atmospheric temperatures and pressures displayed in Fig. 3 is accompanied by a very diverse chemical make-up. In non-irradiated M dwarfs, molecules ( $\text{H}_2$ ,  $\text{H}_2\text{O}$ ,  $\text{CO}$ ,  $\text{TiO}$ , etc.) are the major sources of opacity throughout the atmosphere. For an irradiated atmosphere with  $T_p = 20,000\text{K}$ , the incident flux raises the temperatures in the upper atmosphere so much that most molecules cannot survive. Figure 4 illustrates the changes to the number densities of  $\text{H}_2$ ,  $\text{H}$ ,  $\text{H}^+$ ,  $\text{He}$ , and  $\text{He}^+$ . When  $T_p = 20,000\text{K}$ , the total concentration of molecular species ( $N_{\text{mols}}/N_{\text{gas}}$ ) at  $\tau_{1.2} \leq 10^{-2}$  decreases by more than 5 orders of magnitude compared to the non-irradiated case. Also, a significant fraction of hydrogen is ionized near the top of the atmosphere. When  $T_p > 40,000\text{K}$ , molecules are no longer important in the photosphere and the concentration of  $\text{H}_2$  at the temperature minimum is less than  $10^{-2}$ . Other molecules (e.g.  $\text{CH}_4$  and  $\text{CO}$ ) follow a similar pattern as  $\text{H}_2$  but with

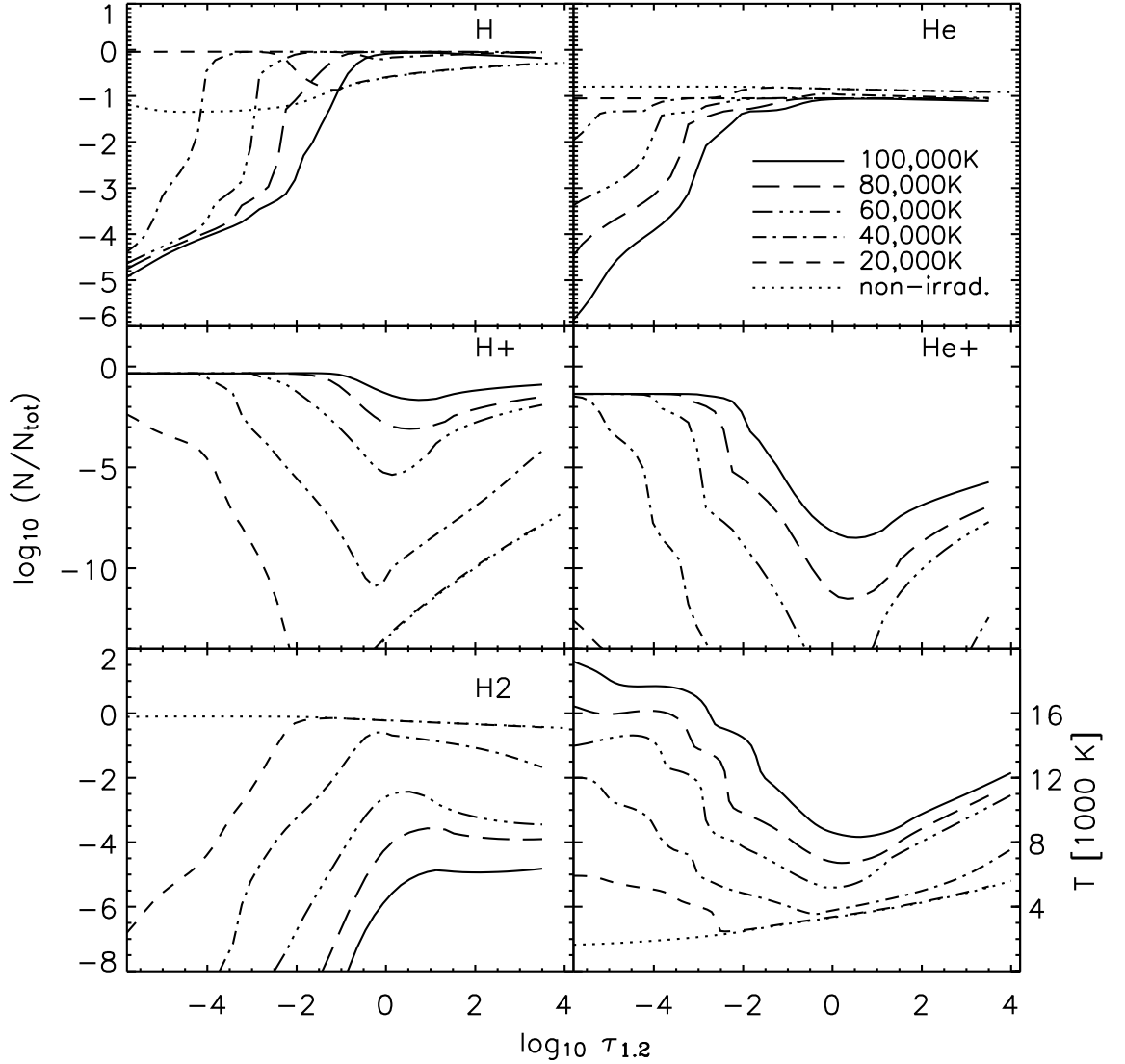


FIG. 4.— The concentrations (number density  $N$  divided by the total number density  $N_{\text{tot}}$ ) of H,  $\text{H}^+$ ,  $\text{H}_2$ , He, and  $\text{He}^+$  are shown for a  $T_{\text{eff}} = 3000\text{K}$  non-irradiated model and the irradiated models with  $T_p = 20,000\text{K}$ ,  $40,000\text{K}$ ,  $60,000\text{K}$ ,  $80,000\text{K}$ , and  $100,000\text{K}$ . The corresponding temperature structures are shown in the bottom right panel.

smaller concentrations at all layers. At even larger  $T_p$ , the atmosphere becomes mostly composed of atoms and ions and, when  $T_p = 100,000\text{K}$ , hydrogen is almost completely ionized down to  $\tau_{1.2} = 0.1$  and He is ionized down to  $\tau_{1.2} = 10^{-2}$ . The ionization in the upper half of the atmosphere dramatically increases the number density of free electrons which, in turn, causes the number density of  $\text{H}^+$  and  $\text{He}^+$  to increase. The heating of the inner atmospheric layers also leads to increased electron densities and concentrations of  $\text{H}^+$  and  $\text{He}^+$ . Overall, the number densities of electrons,  $\text{H}^+$ , and  $\text{He}^+$  follow the same pattern as the temperature structure. Note that, while the solution of the EOS in PHOENIX allows for the possible formation of dust grains and other condensates (as described in Allard et al. 2001), all of the models presented here have atmospheric temperatures that are too hot for grains to form. For intrinsically cooler sec-

ondaries (e.g., brown dwarfs and extrasolar planets) and relatively low irradiation, grain formation will be very important (Barman et al. 2001).

### 3.3. Entropy Matching

The increase in temperature at large depths (i.e., large  $P_{\text{gas}}$ ) and throughout the convection zone has been discussed in previous papers (Vaz & Nordlund 1985; BS93). As described in section 2, the model atmospheres are constrained to be in thermal equilibrium and, therefore, each layer in the convection zone was required to transport a constant total energy. Furthermore, in a purely adiabatic convection zone, the energy transport is determined by the adiabatic temperature gradient. Thus, a temperature increase near the top of the convection zone must lead to an increase at all other layers in the convection zone to ensure a constant luminosity is maintained

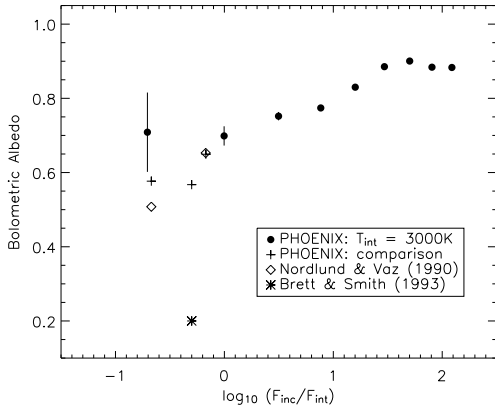


FIG. 5.— The bolometric albedo for the irradiated atmospheres in Fig. 3 (filled symbols). Error bars that assume a 2% error in the net flux of the model are given for each  $T_{\text{int}} = 3000\text{K}$  model. For large  $F_{\text{inc}}$ , the error bars are smaller than the symbol size. Also plotted are albedos from Nordlund & Vaz (1990) (diamonds) and BS93 (asterisk) along with three PHOENIX models (pluses) specifically for comparing with these earlier works.

at all layers of the atmosphere. The now well known consequence of these constraints is that convective irradiated and non-irradiated models with the *same* effective temperature (i.e.  $T_{\text{int}} = T_{\text{eff}}$ ) do not reach the same adiabat at depth (as illustrated in Figs. 2 and 3). Furthermore, since the material below the photosphere is likely to be well mixed, the irradiated and non-irradiated model atmospheres should have the same entropy at depth if they are to represent the two different hemispheres of the same object (Vaz & Nordlund 1985 ; BS93). In most cases, entropy matching can be achieved by lowering  $T_{\text{int}}$  of the irradiated model until the T-P profile matches the non-irradiated model in the convection zone. The difference between  $T_{\text{int}}$  and  $T_{\text{eff}}$  for the matching irradiated and non-irradiated atmospheres is a measure of the bolometric reflection albedo and the energy that is horizontally redistributed in the photosphere (BS93).

The entropy matching technique is designed to mimic the anticipated conditions at large optical depths within the convection zone. These layers should undergo efficient mixing over very short timescales ensuring a constant internal entropy across both hemispheres. Also, the decrease in the atmospheric temperature gradient on the heated hemisphere will slow the rate at which internal energy can escape from that side of the secondary implying a smaller *intrinsic* luminosity on the heated hemisphere compared to the non-heated side. This is consistent with the fact that entropy matching models will always have intrinsic effective temperatures that are less than (or equal to) the  $T_{\text{eff}}$  on the non-irradiated side. Entropy matching, however, cannot deal with the potential horizontal flow of energy in the radiative zones.

To find pairs of entropy matching models, a sequence of non-irradiated models was computed with  $2800\text{K} < T_{\text{eff}} < 6000\text{K}$ . Then, using the entropy at the bottom of an irradiated model, the matching effective temperature ( $T_{\text{matched}}$ ) was found by linearly interpolating along a  $S(T_{\text{eff}})$  curve at the same  $P_{\text{gas}}$  in the non-irradiated models. This method, which is very similar to that described by Vaz & Nordlund (1985), was applied to each of the

models shown in Fig. 3. The matched, non-irradiated, atmospheric structures for the  $T_p = 20,000\text{K}$ ,  $50,000\text{K}$ , and  $100,000\text{K}$  models are also shown as dashed lines and have, respectively,  $T_{\text{eff}} = 3041\text{K}$ ,  $3857\text{K}$ , and  $5910\text{K}$ . Recall that the corresponding irradiated atmosphere models all have  $T_{\text{int}} = 3000\text{K}$ .

The two effective temperature values for the pair of entropy matching models can be used to obtain a value for the bolometric reflection albedo ( $w$ ) via the expression,

$$(1 - w)F_{\text{inc}} = \sigma(T_{\text{matched}}^4 - T_{\text{eff}}^4) \quad (2)$$

(BS93). The albedos versus the ratio of incident to intrinsic fluxes are shown in Fig. 5. For very large incident flux the albedo approaches 1. This is expected since the atmospheres become radiative down to large depths as  $F_{\text{inc}}$  increases. From Fig. 3, the radiative convective boundary is at  $\tau_{1.2} \ll 1$  when  $\log F_{\text{inc}}/F_{\text{int}} > 0.5$ . Atmospheres that are completely in radiative equilibrium have an albedo exactly equal to 1.0 (Eddington 1926). For low incident flux the albedo decreases but is still well above the canonical value of 0.5 for convective atmospheres. In general, the PHOENIX albedos are consistent with the recently published albedos for a variety of models with  $T_{\text{int}} \geq 4000\text{K}$  and  $\log F_{\text{inc}}/F_{\text{int}} \leq 1$  (Claret 2001, Fig. 4).

All models in this paper were considered converged when the flux was conserved to 2% or better at all layers. At this level of convergence, no appreciable improvements in the models are obtained by further iterations. None the less, a small error exists in the net flux of the models which translates into a small error associated with  $T_{\text{matched}}^4$  in eq. 2. For small values of  $F_{\text{inc}}$ , the difference between  $T_{\text{matched}}$  and  $T_{\text{eff}}$  is also small ( $\sim 50\text{K}$ ) which means that even a 2% error in the flux can result in a large error in  $w$ . Error bars corresponding to a 2% error in the model's net flux are shown for each albedo ( $T_{\text{int}} = 3000\text{K}$  models) in Fig. 5. Since the error in  $w$  is also proportional to  $1/F_{\text{inc}}$ , the error bars decrease with increasing  $F_{\text{inc}}$  (and the difference between  $T_{\text{matched}}$  and  $T_{\text{eff}}$  is much larger).

Comparison PHOENIX models were also constructed to match the input parameters of several models from Nordlund & Vaz (1990) (see their Table 2; non-grey models with mixing length parameter equal to 2) in addition to the BS93 models shown in Fig. 2. The PHOENIX albedos for these models are plotted in Fig. 5 and agree well with Nordlund & Vaz (1990) while the BS93 albedo is less than half the value for any of the others. It is difficult to determine the exact reasons why the BS93 result is so much lower than the PHOENIX albedo. In order to obtain an albedo of 0.2 for the PHOENIX model,  $T_{\text{matched}}$  would need to be  $\sim 3800\text{K}$ , instead of the current value of  $\sim 3600\text{K}$ . Note that the BS93 models suffered from many competing simplifications that included SM opacities, the absence of atomic line opacity, and the use of underestimated astrophysical values for the TiO oscillator strengths. The impact of these simplifications can be seen by comparing the BS93 non-irradiated models to Brett's later, much improved, non-irradiated M dwarf models (Brett 1995). The temperature at the bottom of a  $T_{\text{eff}} = 3800\text{K}$  model from Brett (1995) is nearly  $1000\text{K}$  hotter than the bottom of the non-irradiated model shown in BS93 with the same  $T_{\text{eff}}$  (their Fig. 7). However, at  $T_{\text{eff}} = 3400\text{K}$ , the differences at the bottom are on the order of a few  $100\text{K}$ . Using the

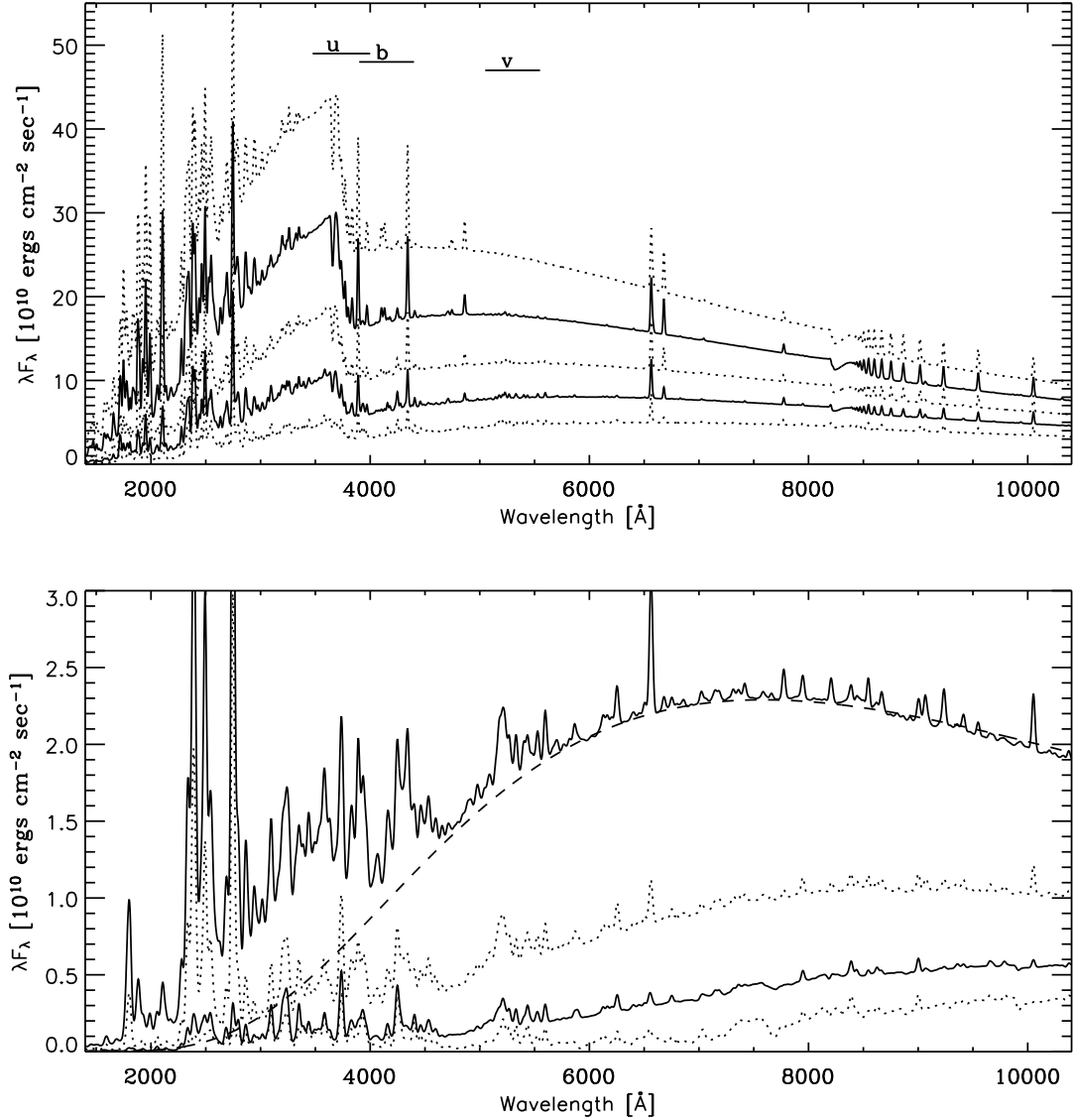


FIG. 6.— Spectra for the irradiated models shown in Fig. 3.  $T_p = 20,000\text{K}$  to  $50,000\text{K}$  in the lower panel and  $T_p = 60,000\text{K}$  to  $100,000\text{K}$  in the upper panel (with  $T_p$  increase from top to bottom). To facilitate comparison, the resolution was reduced to  $15\text{\AA}$  and alternating line styles were used. The dashed line is a best fitting black body spectrum (with  $T_{\text{eff}} = 4840\text{K}$ ) for the  $T_p = 50,000\text{K}$  model.

improved Brett (1995) non-irradiated models to find the  $T_{\text{matched}}$  for the BS93 irradiated model leads to an albedo very comparable to the PHOENIX value. The good agreement in Fig. 2 between the PHOENIX and BS93 irradiated models suggests that, for this particular set of parameters, the extrinsic heating offsets many of the opacity limitations in the BS93 models.

#### 3.4. Synthetic Spectra

The changes to the temperature structure and chemical composition have dramatic consequences for the spectra emerging from the illuminated hemisphere. The synthetic spectra for each of the structures in Fig. 3 are displayed in Fig. 6. The atmospheric model irradiated by the coolest WD ( $T_p = 20,000\text{K}$ ) retains many of the infrared spectral features common to M dwarfs, e.g. TiO and VO absorption bands. However, a substantial

amount of flux emerges at short wavelengths with a dense spectrum of narrow emission lines. As  $T_p$  increases, the flux emerges from two fairly distinct spectral regions divided by a pronounced Balmer-edge at  $3647\text{\AA}$ . When  $T_p$  reaches  $30,000\text{K}$ , the broad spectral features in the red portion of the secondary's spectrum disappear and are replaced by a few narrow emission lines. The blue-UV portions of the spectra, however, have complex mixtures of emission and absorption lines. The strongest of these lines are from Fe I, Fe II, Mg I, Mg II, and Ni I. When  $T_p = 100,000\text{K}$ , many additional emission lines from Fe III, Al II, Ti II, Ni II, and Si I appear in the UV-blue spectrum.

This division of the spectrum into two distinct components is a consequence of the two very different temperature regimes in the atmosphere. The hot, inverted, outer temperature structure produces the blue-UV por-

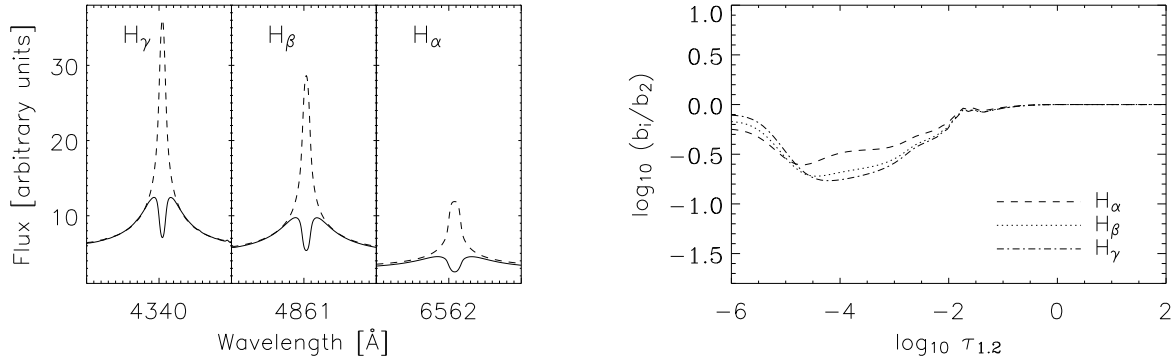


FIG. 7.— Right panel: the ratio of departure coefficients for the levels involving  $H_\alpha$ ,  $H_\beta$ , and  $H_\gamma$  as functions of optical depth at  $1.2\mu\text{m}$ . Each ratio is proportional to the non-LTE line source function. A value other than 1 indicates departure from LTE. Left panel: comparison between LTE (dashed) and non-LTE (solid) line profiles for the corresponding Balmer lines. Each panel is  $20\text{\AA}$  wide.

tion of the spectrum. Note,  $\tau = 1$  at  $3000\text{\AA}$  is at roughly  $\tau_{1.2} = 10^{-4}$ . The red part of the spectrum forms near  $\tau_{1.2} = 1$ , while the core of most emission lines form at smaller  $\tau_{1.2}$ . For all of the cases presented in Fig. 6, the incident radiation is sufficient to produce Balmer, He, and metal emission lines.

A best fitting black body SED, with  $T_{\text{eff}} = 4840\text{K}$ , is also shown in Fig. 6 for  $\lambda \geq 4500\text{\AA}$  and  $T_p = 50,000\text{K}$ . Apart from the emission lines, the red portions of the spectra resemble black body SEDs when  $T_p > 30,000\text{K}$ . This is mostly due to the roughly isothermal  $T-P$  structure near the temperature minimum that occurs close to continuum forming region ( $\tau_{1.2} = 1.0$ ). Spectral features diminish where the temperature structure is flat because the LTE source function cannot vary with depth. At shorter wavelengths, the best fitting black body underestimates the emergent flux by orders of magnitude. Also, for  $T_p \geq 60,000\text{K}$ , a steep Balmer-edge forms in emission. A steep Balmer-edge could explain why, for certain binaries, it is difficult to obtain a single effective temperature for the secondary when using black body SEDs to fit *ubv* photometry.

### 3.5. Hydrogen in non-LTE

A striking feature of the spectra shown in Fig. 6 are the hydrogen emission lines. However, one caveat should be mentioned for the model results discussed so far; in all of the above cases LTE was assumed. Given the *non-local* origin of a primary source of energy (the incident flux), the conditions in the upper atmosphere, where gas pressures are low and temperatures are high, are well suited for significant departures from LTE. To test the importance of non-LTE effects, the  $T_p = 100,000\text{K}$  model was recalculated with neutral Hydrogen allowed to depart from LTE. For this particular test, the Hydrogen model atom included 31 levels, and 435 primary transitions (all bound-bound transitions with  $\log(gf) > -2.0$ ) were included in the solution of the statistical equilibrium equations. For details of the numerical methods used to solve the rate equations, see Hauschildt & Baron (1999).

The LTE and non-LTE line profiles for  $H_\alpha$ ,  $H_\beta$ , and

$H_\gamma$  are compared in Figure 7. Both LTE and non-LTE cases have Balmer wings in emission while dramatic differences exist between the line cores. The non-LTE line profiles all have reversed cores while the LTE lines have cores that are substantially brighter than the non-LTE case. The non-LTE  $H_\alpha$  line core drops slightly below the continuum flux level while the cores of  $H_\beta$ , and  $H_\gamma$  are only slightly above the continuum. The ratio the LTE and non-LTE Balmer line fluxes, for this case, are not significantly different. The non-LTE flux ratio  $H_\alpha/H_\beta$  is  $\sim 0.52$  compared to  $\sim 0.57$  for the LTE case. The non-LTE flux ratios for  $H_\alpha/H_\gamma$  and  $H_\beta/H_\gamma$  are  $\sim 0.41$  and  $\sim 0.80$ , respectively.

In both non-LTE and LTE cases, the line wings form near  $\tau_{1.2} = 1$  while the core of the lines form much higher in the atmosphere near  $\tau_{1.2} = 10^{-4}$ . In LTE, the depth dependent line source function is simply a black body with temperature equal to the local gas temperature. Consequently, the LTE line profile mimics the temperature inversion (top curve in Fig. 3) which changes by  $\sim 9000\text{K}$  between these two optical depths. However, when the LTE approximation is removed, noticeable departures from the LTE atomic level populations occur for the  $n = 2$  level, which is over populated by a factor 10 (compared to the LTE populations) at  $\tau_{1.2} = 10^{-4}$ . The  $n = 1$  and  $3 < n < 6$  levels are also slightly over populated in the upper atmosphere, but less so compared to  $n = 2$ . The non-LTE line source function is not a Planck function, but instead is related to the ratio of the departure coefficients ( $b_i$ 's) for the two levels involved in the transition. The ratio of the  $b_i$ 's for these three Balmer lines are shown in Fig. 7. For all three Balmer lines the ratio of the  $b_i$ 's, and consequently the line source function, decreases in the very region where the line cores form resulting in a fainter core compared to the wings. The LTE and non-LTE profiles are similar in the wings since the  $b_i$ 's approach unity at large optical depth. It is likely that other lines are also affected by non-LTE effects and the authors are working on a future paper that fully explores these issues for a number of atoms and ions.

### 3.6. pre-CV Examples



TABLE 1. SYSTEM PROPERTIES FOR EXAMPLE PRE-CVS

Object	Primary			Secondary			$a(R_\odot)$	$\log(F_{\text{inc}})$	refs.
	$T_{\text{eff}}(K)$	$R(R_\odot)$	$M(M_\odot)$	$T_{\text{eff}}(K)$	$R(R_\odot)$	$M(M_\odot)$			
GD 245	22,170	0.015	0.48	3560	0.27	0.22	1.17	9.35	Schmidt et al. (1995)
NN Ser	55,000	0.019	0.57	2900	0.17	0.12	0.95	11.32	Catalan et al. (1994)
AA Dor	42,000	0.19	0.40	3000	0.10	0.073	1.14	12.69	Hilditch et al. (2003)
UU Sge	85,000	0.34	0.63	6250	0.54	0.29	2.46	13.79	Bell et al. (1994)

The models and methods described above were applied to four example systems (GD 245, NN Ser, AA Dor, and UU Sge) that have been well observed and documented in the literature. These systems were chosen because they represent the broadest range of properties for PCEBs, spanning 4 orders of magnitude in incident flux. Two systems, GD 245 and NN Ser, have WD primaries while the other two, AA Dor and UU Sge, have hot sub-dwarf stars as primaries. The purpose of this section is not to determine the properties of each system, but instead to illustrate some of the probable characteristics of their secondary's heated hemisphere. The orbital parameters and the bulk properties for the primary and secondary were taken from previous works and are listed in Table 1.

### 3.6.1. GD 245 & NN Ser

GD 245 and NN Ser are two examples of pre-CVs for which phase resolved spectroscopy has been performed (Schmidt et al. 1995; Catalan et al. 1994). Both systems are observed to have Balmer lines composed of absorption wings from the primary and narrow emission cores from the heated face of the secondary. The strength of the emission peaks at zero phase when the heated hemisphere is most visible. The observations of GD 245 clearly show the presence of additional emission lines from the secondary due to various metals (Mg II, Fe I, Na I, and Ca II). The spectra of NN Ser also show the presence of emission from Ca II and He I. Using the parameters listed in Table 1, model atmospheres were computed for the secondary of both GD 245 and NN Ser. As described above, a single irradiated model was used to represent the average properties of the heated hemisphere.

The temperature structures are shown in Fig. 8. Both GD 245 and NN Ser have substantial temperature inversions at the top of the atmosphere and, in the case of NN Ser, extending down to  $\tau_{1.2} = 1$ . Both structures are compared to that of a non-irradiated M dwarf with  $\log(g) = 5.0$  and  $T_{\text{eff}} = 3500K$  (lowest dashed curve in Fig. 8). Apart from the temperature inversion, the irradiated model of GD 245 remains similar to a normal M dwarf atmosphere with convection present at layers where  $\tau_{1.2} < 0.1$ . However, the model for NN Ser, which included a much hotter primary ( $T_p = 55,000K$ ) than GD 245, has a purely radiative atmosphere and is nearly isothermal down to  $\tau_{1.2} = 1$ .

In the lower panel of Fig. 9, a *total* synthetic spectrum is shown for the GD 245 system: i.e. the spectrum of the WD primary and heated face of the secondary were added using the parameters listed in Table 1 assuming a  $90^\circ$  inclination. At  $\lambda \lesssim 6000\text{\AA}$ , the pseudo-

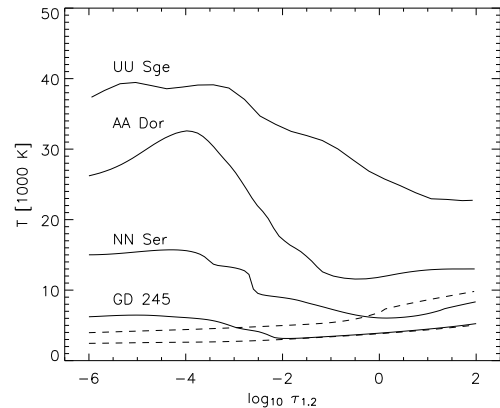


FIG. 8.— Temperature versus optical depth (at  $1.2\mu\text{m}$ ) from irradiated models for the example cases listed in Table 1 (solid lines). Dashed lines are non-irradiated models with  $T_{\text{eff}} = 6000K$  (top) and  $T_{\text{eff}} = 3000K$  (bottom).

continuum is shaped primarily by the WD's continuum and broad Balmer absorption lines. The red part of the spectrum is dominated by the flux from the secondary, which retains deep molecular absorption bands despite the extrinsic heating. In addition, the synthetic spectrum approximately reproduced the basic collection of emission lines and relative line strengths shown in previously published observed spectra (see Figs. 2 and 3 of Schmidt et al. 1995). There are certainly differences between the observed spectrum and the synthetic spectrum (e.g., the number and widths of the metal lines). However, given that only a single 1-D model was used for the secondary's heated hemisphere and only Hydrogen was treated in non-LTE, the similarities are encouraging. Also, Schmidt et al. (1995) estimated that GD 245 emits about 60 times more  $H_\alpha$  flux than predicted by simply counting the raw number of incident ionizing photons from the WD. Schmidt et al. (1995) suggested that irradiation might reduce the number densities of molecular and neutral atomic opacity sources and allow for the WD's Balmer continuum to supply the photons needed to explain the  $H_\alpha$  flux. This idea is supported by the current models, which do show a dramatic decrease in the concentration of molecules and neutral atomic species. Furthermore, the synthetic spectrum shown in Fig. 9 has  $H_\alpha$  flux  $\sim 2 \times 10^{-14} \text{ ergs cm}^{-2} \text{ sec}^{-1}$  which is close to the observed value of  $3.7 \times 10^{-14} \text{ ergs cm}^{-2} \text{ sec}^{-1}$  at phase zero. Note that a more realistic synthetic spectrum built from many irradiated models that simulate the variable heating across the secondary's surface reproduces the ob-

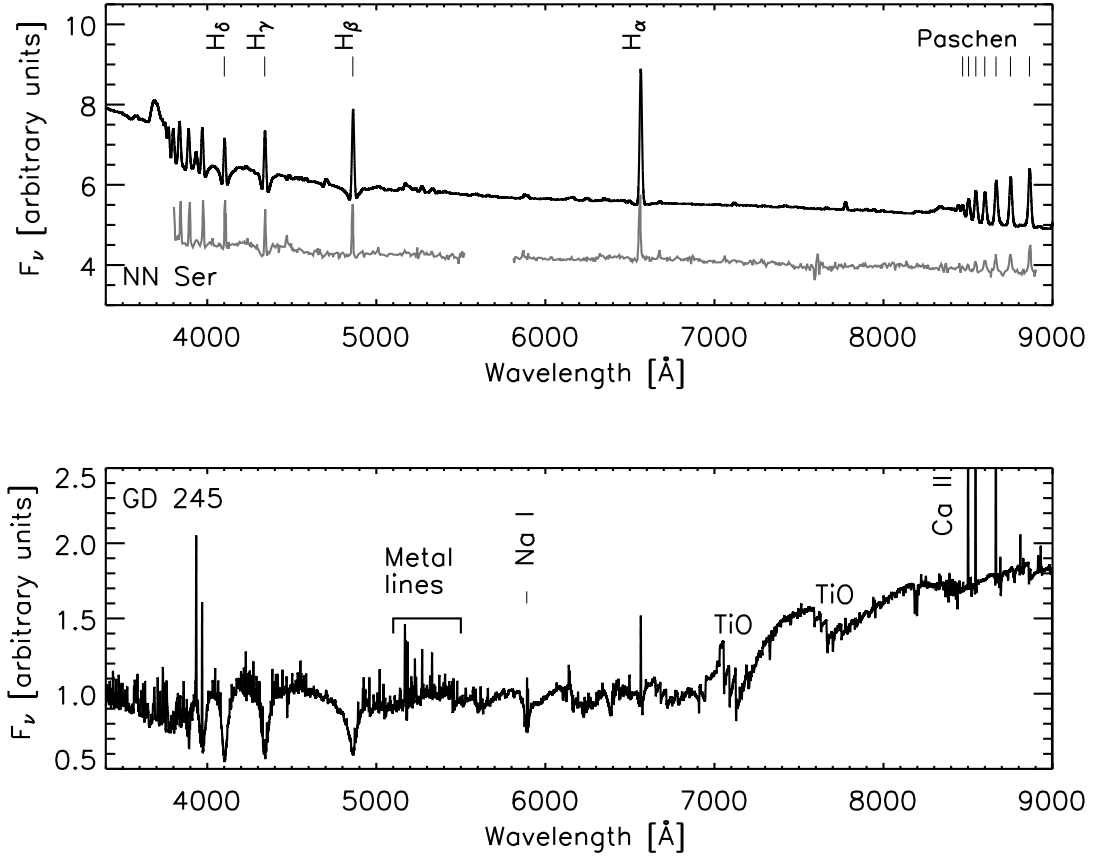


FIG. 9.— Combined spectra, i.e. primary flux plus the flux from the irradiated hemisphere of the secondary, for NN Ser (top) and GD 245 (bottom). The atmospheric structures for the irradiated model atmospheres are shown in Fig. 8. The primary and secondary spectra were combined assuming an orbital inclination of  $90^\circ$  and phase 0. Note, both figures were designed to mimic those shown in Schmidt et al. (1995) and Catalan et al. (1994) to facilitate a comparison. Furthermore, both secondary spectra were rotationally broadened using  $V_{\text{rot}} = 70 \text{ km sec}^{-1}$  and the resolution was reduced to  $5\text{\AA}$  for NN Ser and  $2\text{\AA}$  for GD 245 to matched the observed spectral resolutions from these studies. In the top panel, an observed spectrum of NN Ser from Catalan et al. (1994) is also shown, but offset to make the plot more readable. Note, that the meanings of phases 0 and 0.5 are reversed in the Catalan et al. (1994) paper compared the present work.

served Balmer line profiles of GD 245 very well (Barman 2002).

The temperature structure of the heated hemisphere in NN Ser is significantly different from that of any non-irradiated main sequence star. The hot WD flux heated the secondary enough to suppress convection below the photosphere and reduced the presence of most molecules to very low concentrations. The combined WD + M dwarf synthetic spectrum for NN Ser is shown in Fig. 9 (top panel) assuming a  $90^\circ$  inclination. As with GD 245, the flux from the hot primary determined most of the pseudo-continuum while narrow Balmer and Paschen lines filled in the cores of the WD hydrogen absorption lines. Also shown in Fig. 9 is a digitized version of the observed spectrum of NN Ser published by Catalan et al. (1994) for a similar phase. As with GD 245, the synthetic spectrum is very comparable to the observed spectrum of NN Ser. The pseudo-continuum and most emission lines are well reproduced by the model. The most noticeable differences are the strengths of the H emission lines which are weaker in the red half of the observed data. It should be stressed that no attempt has been made yet to find the best-fitting model for the observed spectrum. This

comparison is simply for illustrative purposes and a more detailed analysis of observed spectra will be the subject of a later paper.

### 3.6.2. AA Dor & UU Sge

AA Dor and UU Sge are examples of extreme irradiation. The primaries, in both cases, are hot sub-dwarfs with radii more than an order of magnitude larger than the WD primaries of GD 245 and NN Ser. Furthermore, the primary of UU Sge is extremely hot,  $T_p = 85,000\text{K}$ . The atmospheric structures for the heated hemispheres of UU Sge and AA Dor are shown in Fig. 8. Both models have large temperature inversions and are radiative to depths well below the photosphere. Temperatures in AA Dor rise by nearly  $20,000\text{K}$  between  $\tau_{1.2} = 1$  and  $\tau_{1.2} = 10^{-4}$ . In the heated hemisphere model for UU Sge, temperatures are well above  $20,000\text{K}$  with a maximum temperature near  $\tau_{1.2} = 10^{-4}$  of almost  $40,000\text{K}$ . The impact of this heating is also evident in their spectra. Figure 10 shows the flux from the heated hemisphere model only; for these systems the dominant flux is from the primary and the secondary simply makes a small contribution to the overall pseudo-continuum. As in Fig. 6,

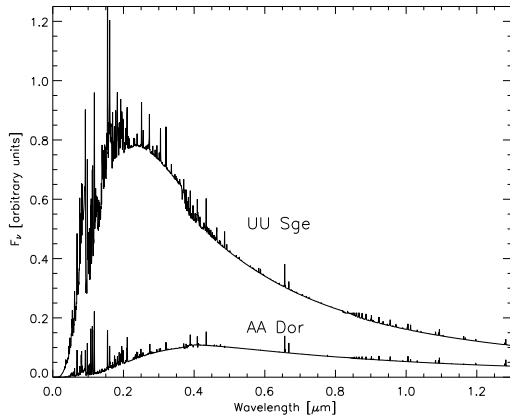


FIG. 10.— Spectra for the irradiated hemispheres of AA Dor and UU Sge. The atmospheric structures for the irradiated model atmospheres are shown in Fig. 8. For both spectra, the resolution was reduced to  $5\text{\AA}$ .

a number of emission lines form in the bluest parts of the spectrum.

Based on light curve analyses, it has been estimated that the temperature varies from 20,000K and 2000K across the heated and non-heated faces of AA Dor (Hilditch et al. 2003). Such a difference is consistent with the irradiated and non-irradiated structures from Fig. 8 (keeping in mind that the models are averages for each hemisphere). The light curve analyses also suggest that the albedo is very close to one (Hilditch et al. 2003) which is also consistent with the model being fully radiative (and Fig. 5).

#### 4. DISCUSSION AND CONCLUSIONS

Model atmospheres have been computed for irradiated stars in pre-CV systems and high-resolution synthetic spectra are now available for direct comparison to observations. The models presented above illustrate the dramatic differences that may exist between the heated and non-heated hemispheres of the secondary in pre-CV systems. Large temperature inversions, which can extend down to the continuum forming layers of the photosphere, are predicted on the heated hemisphere. Such temperature inversions naturally lead to emergent spectra that are unlike normal main sequence stars and are very different from black bodies. A steep Balmer-edge and strong hydrogen emission lines are present in addition to a forest of narrow metal lines in emission. It has also been shown that departures from LTE are to be expected and can have significant impact on the hydrogen line profiles. The present models are consistent with previous findings for the atmospheric structures and bolometric reflection albedos (Vaz & Nordlund 1985; Nordlund & Vaz 1990; BS93).

The large differences between the irradiated and non-irradiated atmosphere models suggest that steep horizontal temperature and pressure gradients may exist across

the surface of a pre-CV secondary. If present, the secondary's heated hemisphere will have a SED that varies substantially across the heated surface, which may be underrepresented by single 1-D averaged models. Such gradients could also lead to strong horizontal flows and redistribution of energy to the non-irradiated hemisphere (Kirbiyik & Smith 1976; Beer & Podsiadlowski 2002). Furthermore, these gradients may lead to convectively unstable layers above the radiative-convective boundary predicted by the mixing length theory. The present work will be expanded to include full surface modeling of pre-CV secondaries in order to compute even more realistic light curves and synthetic spectra.

A detailed non-LTE analysis is currently underway for a large number of atoms and ions for the strongly irradiated systems. For the cooler cases that still have significant concentrations of molecules in their atmosphere, solving the rate equations is a very challenging problem. Much of the atomic and molecular data (e.g. collisional cross-sections for atom/ion plus molecule interactions) are not yet available and are difficult to obtain. However, some useful limits can be placed on the magnitude of the non-LTE effects for such cases.

High-resolution, phase-resolved, spectra have been recently obtained for several interesting pre-CVs (Exter et al. 2003a,b) and a future paper will be devoted to an analysis of these systems using synthetic spectra from irradiated model atmospheres. The example pre-CV systems described above are also prime candidates for detailed comparisons between observed spectra and synthetic spectra. In addition to providing insight into the atmospheric conditions of irradiated M dwarfs, such comparisons will also provide valuable tests for the modeling techniques that are currently being used in other areas (e.g. White Dwarf – Brown Dwarf pairs and close-in extrasolar planets).

T. B. wishes to thank Katrina Exter and David Alexander for many useful discussions during the course of this work. This research was partially supported by the CNRS and NASA LTSA grant NAG5-3435 to Wichita State University. T. B. also acknowledges support by NASA through the American Astronomical Society's small research grant program. Some of the calculations presented in this paper were performed on the IBM pSeries of the HLRN, the IBM SP of the San Diego Supercomputer Center (SDSC) with support from the National Science Foundation, the IBM SP of the NERSC with support from the DoE, and the Wichita State University High Performance Computing Center with the support of Kansas NSF Cooperative Agreement EPS-9874732. We thank all these institutions for a generous allocation of computer time.

#### REFERENCES

- Allard, F., Hauschildt, P. H., Alexander, D. R., Tamanai, A., & Schweitzer, A. 2001, *ApJ*, 556, 357  
 Aufdenberg, J. P. 2001, *PASP*, 113, 119  
 Barman, T. S. 2002, PhD thesis, University of Georgia  
 Barman, T. S., Hauschildt, P. H., & Allard, F. 2001, *ApJ*, 556, 885  
 Barman, T. S., Hauschildt, P. H., Schweitzer, A., Stancil, P. C., Baron, E., & Allard, F. 2002, *ApJ*, 569, L51

- Barman, T. S., Hauschildt, P. H., Short, C. I., & Baron, E. 2000, *ApJ*, 537, 946
- Beer, M. E. & Podsiadlowski, P. 2002, *MNRAS*, 335, 358
- Bell, S. A., Pollacco, D. L., & Hilditch, R. W. 1994, *MNRAS*, 270, 449
- Brett, J. M. 1995, *A&AS*, 109, 263
- Brett, J. M. & Smith, R. C. 1993, *MNRAS*, 264, 641
- Catalan, M. S., Davey, S. C., Sarna, M. J., Cannon-Smith, R., & Wood, J. H. 1994, *MNRAS*, 269, 879
- Claret, A. 2001, *MNRAS*, 327, 989
- Eddington, A. S. 1926, *MNRAS*, 86, 320
- Exter, K., Pollacco, D. L., Maxted, P. F. L., Napiwotzki, R., & Bell, S. A. 2003a, in *NATO ASIB Proc. 105: White Dwarfs*, 287–+
- Exter, K. M., Pollacco, D. L., & Bell, S. A. 2003b, *MNRAS*, 341, 1349
- Ferguson, D. H. & James, T. A. 1994, *ApJS*, 94, 723
- Gruszka, M. & Borysow, A. 1997, *Icarus*, 129, 172
- Hauschildt, P. H., Allard, F., & Baron, E. 1999, *ApJ*, 512, 377
- Hauschildt, P. H. & Baron, E. 1999, *JCAM*, 102, 41
- Hilditch, R. W., Kilkenny, D., Lynas-Gray, A. E., & Hill, G. 2003, *MNRAS*, 344, 644
- Hillwig, T. C., Honeycutt, R. K., & Robertson, J. W. 2000, *AJ*, 120, 1113
- Husson, N., Bonnet, B., Scott, N., & A., C. 1992, *JQSRT*, 48, 509
- Kirbiyik, H. & Smith, R. C. 1976, *MNRAS*, 176, 103
- Kurucz, R. L. 1993, *Molecular Data for Opacity Calculations*, Kurucz CD-ROM No. 15
- . 1994, *Atomic Data for Fe and Ni*, Kurucz CD-ROM No. 22
- Kurucz, R. L. & Bell, B. 1995, *Atomic Line List*, Kurucz CD-ROM No. 23
- Marsh, T. R. 2000, *New Astronomy Review*, 44, 119
- Nordlund, A. & Vaz, L. P. R. 1990, *A&A*, 228, 231
- Paczynski, B. 1980, *Acta Astronomica*, 30, 113
- Partridge, H. & Schwenke, D. W. 1997, *J. Chem. Phys.*, 106, 4618
- Rothman, L. S., Gamache, R. R., Tipping, R. H., Rinsland, C. P., Smith, M. A. H., Chris Benner, D., Malathy Devi, V., Flaub, J.-M., Camy-Peyret, C., Perrin, A., Goldman, A., Massie, S. T., Brown, L., & Toth, R. A. 1992, *JQSRT*, 48, 469
- Schmidt, G. D., Smith, P. S., Harvey, D. A., & Grauer, A. D. 1995, *AJ*, 110, 398
- Schwenke, D. W. 1998, *Chemistry and Physics of Molecules and Grains in Space. Faraday Discussion*, 109, 321
- Vaz, L. P. R. & Nordlund, A. 1985, *A&A*, 147, 281